Supplementary Information

The Formation of Silicate-Stabilized Passivating Layers on Pyrite for Reduced Acid Rock Drainage

R. Fan[a], M. D. Short[a], S. J. Zeng[a], G. Qian[a], J. Li[a], R. C. Schumann[b], N. Kawashima[c], R. St.C. Smart[a,d] and A. R. Gerson[d*]

[a] School of Natural and Built Environments, University of South Australia, Mawson Lakes, South Australia 5095, Australia;

[b] Levay & Co. Environmental Services, Edinburgh, South Australia 5111, Australia;

[c] Future Industries Institute; University of South Australia, Mawson Lakes, SA 5095, Australia

[d] Blue Minerals Consultancy, Middleton, SA 5213, Australia

*Corresponding author: Tel.: 61 422 112 516;

Email: andrea@bluemineralsconsultancy.com.au

Cover sheet

Tables:

Figures:

S1 Surface analyses

Solid samples to be examined by scanning electron microscopy (SEM) and energy dispersive X-ray spectroscopy (EDS) were vacuum dried at 40 °C overnight and then stored in sealed containers (<1 h) flushed with argon gas (Ar, 99.9 %) at room temperature. Dry particles were mounted on pin-type aluminium SEM stubs with double-sided conducting carbon adhesive and coated with carbon to minimise surface charging. SEM imaging was carried out using a Quanta 450 FEG with accelerating voltage of 15 kV, continuous adjustable probe current ≤ 200 nA and magnification of 6 to 1,000,000. This SEM is equipped with an energy dispersive spectroscopy detector to enable semi-quantitative determination of chemical composition. The working distance was kept at 10 mm. The EDS is equipped with an ultra-thin beryllium window to analyse low energy X-ray fluorescence, such as from C and O.

TEM samples were prepared using a dual-beam FIB/SEM (FEI Helios Nanolab 600) with in situ lift out technique. The sample was placed in the sample holder with the help of conductive glue (silver) before sputter coating with carbon. A layer of platinum was deposited to protect the sample surface for selective milling. Milling was performed under vacuum using a high energy gallium ion beam, with real time monitoring of both electron and ion beams. High current (21 nA at 30 kV) was used for rough milling followed by gentle polishing with subsequent low currents (6.5 nA, 2.8 nA, 0.92 nA, 0.28 nA and 93 pA at 30 kV). TEM bright-field images and electron diffraction patterns were subsequently obtained with a Tecnai (FEI) G2 Spirit operated at 120 kV.

S2 Statistical analyses

Univariate linear regression was used to interrogate pyrite dissolution kinetics for the various pH and silicate treatment combinations. Differences between dissolution rates (i.e. slopes of significantly linear regression lines), verified via runs testing[1] with and without silicate addition at either pH 3.0, 5.0 or 7.4, were assessed by Analysis of Covariance (ANCOVA)[2], with level of statistical significance given alongside corresponding F test statistic. Normality of residuals for regression analyses were verified ($p > 0.05$) via Shapiro–Wilk's test. Differences in pyrite dissolution rates for each treatment (with and without silicate addition) across all three pH conditions were assessed by non-parametric Kruskal–Wallis testing with Dunn's *post hoc* tests for multiple comparisons. Non-parametric analysis was applied here over equivalent parametric ANOVA due to small sample size ($n = 3$) and associated inability to validate prerequisite parametric data normality assumptions. Level of statistical

significance for multiple comparisons (Dunn's test) is given alongside the Kruskal–Wallis test statistic (H) at alpha significance level 0.05. Parametric Pearson's correlation analysis was used to assess relationships between treatment pH and iron, or silicate dissolution/precipitation kinetics following data transformation (log(x)) to satisfy underlying normality assumptions (Shapiro–Wilk's test).

S3 Pyrite dissolution

Table 1 Pyrite dissolution rates (± 1 SE) with and without silicate (0.8 mM Si) addition at pH 3.0, 5.0 and 7.4. Dissolution rates derived from linear regression of dissolved S concentration as a function of time. Differences between dissolution rates with and without Si addition determined by ANCOVA.

Conditions	**Pyrite dissolution rate (mol m^{-2} s^{-1})**	**Rate difference with Si**
pH 3.0	2.70×10^{-11} ($\pm$ 9.7×10^{-13})	ns
pH 3.0 +Si	2.65×10^{-11} ($\pm$ 7.9×10^{-13})	$F_{(1,14)} = 0.1608$; $p = 0.6945$
pH 5.0	3.81×10^{-11} ($\pm$ 1.4×10^{-12})	***
pH 5.0 +Si	2.89×10^{-11} ($\pm$ 1.3×10^{-12})	$F_{(1,14)} = 23.642$; $p = 0.00025$
pH 7.4	5.00×10^{-11} ($\pm$ 9.3×10^{-13})	****
pH 7.4 +Si	5.97×10^{-13} ($\pm$ 3.6×10^{-13})	$F_{(1,14)} = 2447.4$; $p < 0.0001$

S4 Electron diffraction patterns of surface layers at pH 7.4

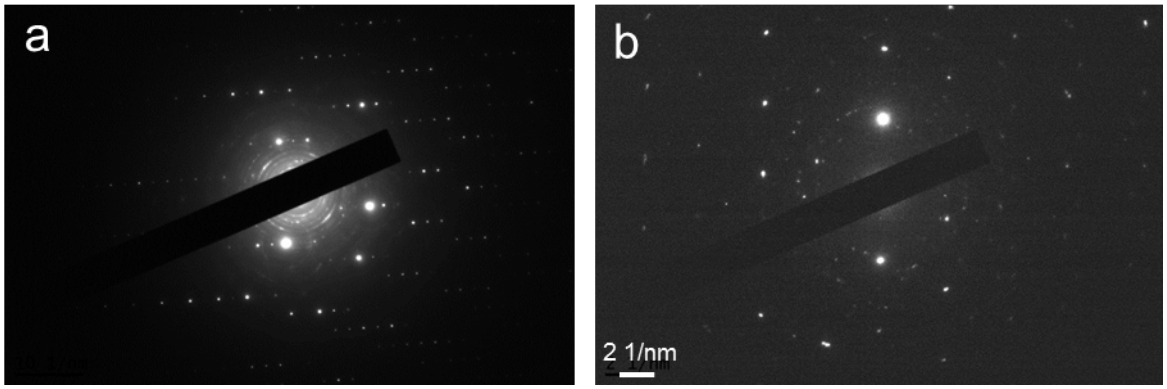

Figure 1 Electron diffraction patterns of pyrite and the corresponding surface layers formed in neutral solution over 290 days with no added silicate (a) and added silicate (b). Discrete diffraction spots, corresponding to single crystal pyrite grains, were observed in both (a) and (b). Diffraction rings in (a) correspond to polycrystalline goethite particles.

S5 Density functional theory (DFT) computational simulation

Ferrihydrite is often suggested to be one of the common reaction products (or an intermediate product) of pyrite oxidation under aqueous conditions.[3-8] In particular, Hood [9] investigated the dissolution kinetics of pyrite at 10–55 °C and pH 7–9, and found that (two-line) ferrihydrite was exclusively formed in the presence of silica (dissolved from glass reaction vessels). Based on these earlier studies and the conditions (circum-neutral pH with added silicate) for the formation of silicate-stabilised 'Fe(III) (oxy)hydroxide' in this work, we adopted two-line ferrihydrite as a model to represent the amorphous Fe(III) (oxy)hydroxide pyrite surface passivation layer for preliminary density functional theory (DFT) modelling.

DFT computational simulation was carried out at absolute zero (0 K) using the Vienna Ab-initio Simulation Package (VASP) code (version 5.3.5) with a projector-augmented wave method (PAW) and plane wave basis set,[10] and the general gradient approximation-type Perdew-Burke-Ernzerhof functional. The initial unit cell structure of ferrihydrite was constructed based on previous publications.[11, 12] A Monkhorst-Pack *k*-point mesh of 8×8×4 was used for numerical integration over the Brillouin zone for the ferrihydrite unit cell. The plane wave basis was truncated with an energy cut-off at 480 eV for all the VASP calculations (i.e. all plane waves with kinetic energies <480 eV are included in the basis set for calculations).

Si-doped ferrihydrite was simulated using a 2×2 supercell of the refined two-line ferrihydrite structure. TEM-EDS analysis of the surface passivation layers indicates that the coating contains 24 at.% Fe and 1.1 at.% Si (Si/(Si+Fe) = 0.04). To be comparable, two Si atoms were substituted for two Fe of the 40 Fe atoms in the un-doped ferrihydrite supercell resulting in Si_{Fe} point defects of molar ratio Si/(Si+Fe)=2/(2+38)=0.05. One Si was placed in tetrahedral and one in octahedral coordination. The energy cut-off at 480 eV and a Monkhorst-Pack *k*-point mesh of 4×4×2 were adopted for the simulation of Si-doped ferrihydrite.

For refinement of the ferrihydrite unit cell all atoms and unit cell parameters were allowed to move/vary (ISIF=3; see VASP manual http://cms.mpi.univie.ac.at/vasp/vasp.pdf) while maintaining symmetry and unit cell constraints as defined by the ferrihydrite space group (ISYM=2; i.e. default setting for the PAW method). This resulted in unit cell parameters of a = b = 5.723 Å, and c = 8.881 Å; α = β = 90°, and γ = 120°. The same key-words were applied to the Si-doped 2×2 ferrihydrite supercell (initially a = b = 11.446 Å , c = 8.881, α = β = 90°, γ = 120°). However, in this instance the space-group symmetry was broken by the presence of the two Si atoms and the atomic positions and supercell parameters refined freely (a = 11.304 Å, b = 11.396 Å, c= 8.770 Å, α = 89.44°, β = 90°, γ = 119.73°). The refined structures for the undoped ferrihydrite unit cell and the Si doped supercell are shown in Figures 2 and 3, respectively with the fractional coordinates of the refined Si-doped supercell provided in Table 2.

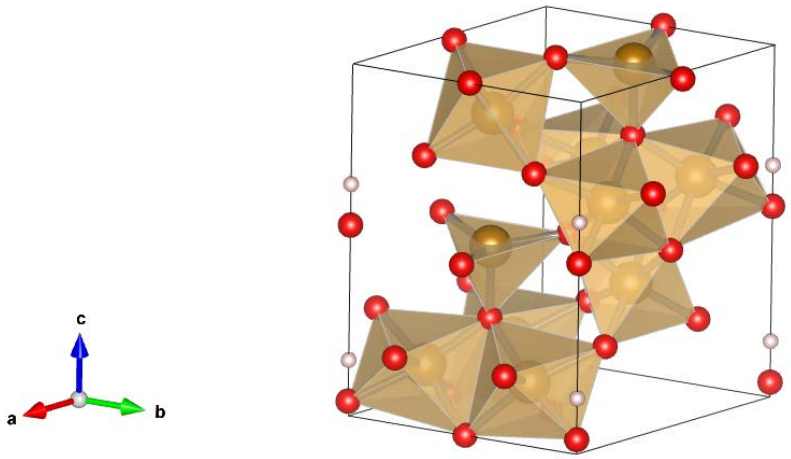

Figure 2 The refined unit cell of two-line ferrihydrite. (Fe – yellow spheres, O – red spheres, H – white spheres)

The total formation energies of two Si_{Fe} defects were calculated based on equation 1:

$$E_{de} = E_s(2Si) + 2E(Fe) – E_s – 2E(Si) \quad (1)$$

in which E_{de} is the total energy of formation of the two Si_{Fe} defects, $E_s(2Si)$ and E_s are the total energies of the 2×2 ferrihydrite supercell with (−788.33 eV) and without (−777.20 eV) two Si_{Fe} defects, E(Fe) and E(Si) are the total energies of Fe (−3.19 eV) and Si (−0.88 eV) atoms.

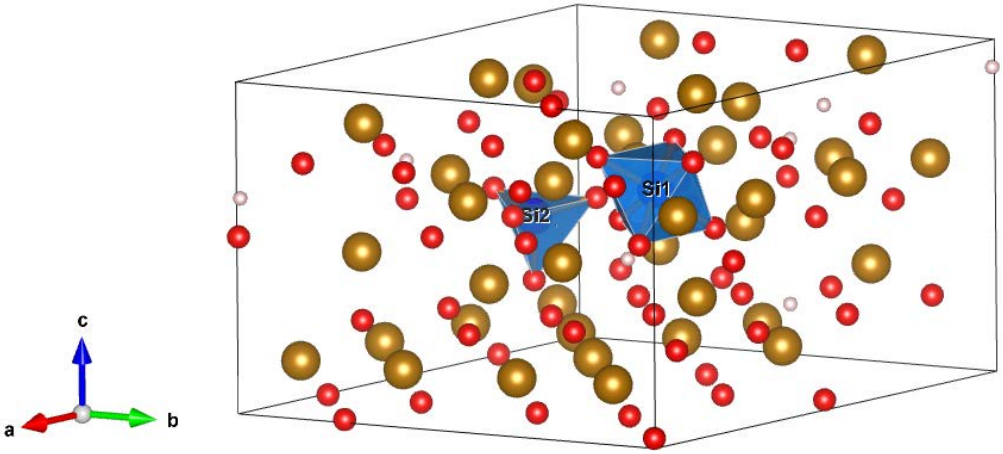

Figure 3 Schematic representation of refined structural model with two Si atoms replacing Fe within the structure of 2×2 ferrihydrite supercell. (Fe – brown spheres, O – red spheres, H – white spheres, Si – blue spheres located within the blue pyramid and tetrahedra)

Although this specific Si-doped two-line ferrihydrite model represents only one possible structure, inclusion of this preliminary DFT modelling provides initial theoretical insights into understanding of the thermodynamic stability of both Si-doped and undoped structures. It is acknowledged that variations of the initial structure for DFT calculation (e.g. location of Si in the supercell) or calculation of the defect formation energy (Eq. 1; S5) using other possible Si or Fe species, will likely affect modelling results. Future research would require the use of EXAFS (to determine the structural coordination of impurity ions, i.e. Si in this case, as has been widely used [13-15]) in conjunction with DFT modelling for more detailed understanding. [16]

Table 2 Cartesian coordinates of atoms for the refined Si-doped 2×2 supercell of two-line ferrihydrite.

Atom	x	y	z	Atom	x	y	z
Fe_1	-1.29608	4.07712	5.60689	O_{19}	4.26697	4.08878	2.10640
Fe_2	-4.19960	9.11767	5.72596	O_{20}	1.47901	9.01333	2.14134
Fe_3	4.20250	4.18750	5.67409	O_{21}	-0.01875	1.66659	2.09516
Fe_4	1.53843	9.06870	5.68799	O_{22}	-2.82612	6.71395	2.10651
Fe_5	-0.04249	1.84616	5.67176	O_{23}	5.67101	1.66659	2.09516
Fe_6	-2.82612	6.92118	5.56592	O_{24}	2.82613	6.45557	2.34669
Fe_7	5.69474	1.84616	5.67176	O_{25}	1.38528	4.08878	2.10640
Fe_8	1.44975	4.18750	5.67409	O_{26}	-1.42148	9.07477	2.10100
Fe_9	-1.45265	9.11767	5.72596	O_{27}	7.01505	4.10954	2.11187
Fe_{10}	6.94833	4.07712	5.60689	O_{28}	4.17324	9.01334	2.14134
Fe_{11}	4.11382	9.06870	5.68799	O_{29}	4.29236	0.90670	6.61353
Fe_{12}	4.25910	0.81082	1.26323	O_{30}	1.55321	5.84839	6.60990
Fe_{13}	1.35574	5.77268	1.33715	O_{31}	9.82437	0.94765	6.51811
Fe_{14}	9.86437	0.79436	1.29644	O_{32}	6.79948	6.00121	6.21860
Fe_{15}	6.89058	5.86199	1.29309	O_{33}	2.82612	3.37619	6.58339
Fe_{16}	2.82612	3.30291	1.26123	O_{34}	0.04523	8.35964	6.60359
Fe_{17}	0.02183	8.20040	1.35281	O_{35}	8.47837	3.37438	6.50897
Fe_{18}	8.47837	3.22269	1.28612	O_{36}	5.60702	8.35964	6.60359
Fe_{19}	5.63042	8.20040	1.35281	O_{37}	1.35989	0.90670	6.61353
Fe_{20}	1.39315	0.81082	1.26323	O_{38}	-1.14722	6.00121	6.21860
Fe_{21}	-1.23833	5.86199	1.29309	O_{39}	7.13238	0.94765	6.51811
Fe_{22}	7.09238	0.79436	1.29644	O_{40}	4.09904	5.84839	6.60990
Fe_{23}	4.29651	5.77268	1.33715	O_{41}	1.57096	2.37931	0.06614
Fe_{24}	0.00543	3.27857	3.03793	O_{42}	-1.23263	7.42867	8.76821
Fe_{25}	-2.82612	8.34920	3.04039	O_{43}	7.21206	2.37962	0.03387
Fe_{26}	5.64682	3.27857	3.03793	O_{44}	4.36683	7.30463	0.11648
Fe_{27}	2.82613	8.21797	3.16084	O_{45}	2.82613	0.16760	0.07525
Fe_{28}	2.82612	1.73732	7.50839	O_{46}	0.02249	5.21886	8.76937
Fe_{29}	0.05057	6.71333	7.50712	O_{47}	8.47838	0.17103	0.02659
Fe_{30}	8.47837	1.78044	7.49625	O_{48}	5.62976	5.21886	8.76937
Fe_{31}	5.60168	6.71333	7.50712	O_{49}	4.08129	2.37931	0.06614
Fe_{32}	0.00073	3.40520	8.48994	O_{50}	1.28542	7.30463	0.11648
Fe_{33}	-2.82612	8.29940	8.54115	O_{51}	9.74469	2.37962	0.03387
Fe_{34}	5.65152	3.40520	8.48994	O_{52}	6.88488	7.42867	8.76821
Fe_{35}	2.82613	8.33629	8.53791	O_{53}	1.44501	2.52535	4.41807

Fe_{36}	-0.19707	6.50205	4.27107	O_{54}	-1.55302	7.72225	4.38575
Fe_{37}	8.47837	1.62676	4.07685	O_{55}	6.93035	2.57981	4.37183
Fe_{38}	5.84932	6.50205	4.27107	O_{56}	4.06843	7.44091	4.59889
O_1	5.64364	9.85288	0.25714	O_{57}	0.09298	4.69286	4.38322
O_2	-2.82612	4.99387	0.32283	O_{58}	2.82612	0.08172	4.43998
O_3	0.00861	9.85288	0.25714	O_{59}	5.55927	4.69286	4.38322
O_4	2.82613	4.98517	0.29655	O_{60}	2.82612	9.71045	4.38798
O_5	11.26836	0.07272	4.67360	O_{61}	-1.27810	2.57981	4.37183
O_6	-2.82612	5.02527	4.69095	O_{62}	-4.09922	7.72224	4.38575
O_7	5.68839	0.07272	4.67360	O_{63}	4.20725	2.52535	4.41807
O_8	2.82612	5.15957	4.60607	O_{64}	1.58382	7.44090	4.59889
O_9	0.08988	3.40353	6.68663	Si_1	2.82613	6.60061	5.67343
O_{10}	-2.82612	8.38868	6.74132	Si_2	2.82612	1.68723	4.01014
O_{11}	5.56237	3.40353	6.68663	H_1	-5.61248	9.94614	8.03898
O_{12}	2.82613	8.12827	6.69367	H_2	-2.82612	5.06170	1.33317
O_{13}	2.82612	1.65302	2.32533	H_3	-0.03977	9.94614	8.03898
O_{14}	0.04651	6.63440	2.42811	H_4	2.82613	5.17211	8.07582
O_{15}	8.47837	1.61186	2.27018	H_5	11.23219	0.11951	5.69227
O_{16}	5.60574	6.63440	2.42811	H_6	-2.82612	5.14339	5.69571
O_{17}	-1.36280	4.10954	2.11187	H_7	5.72456	0.11951	5.69227
O_{18}	-4.23076	9.07477	2.10100	H_8	2.82612	5.44345	3.61496

Data availability. Underlying data which support the findings of this study are available from:
Collection − https://researchdata.ands.org.au/long-term-acid-source-control/794687
Dataset− https://researchdata.ands.org.au/long-term-acid-source-control/794688

References

1. Bradley, J. V., Distribution-free statistical tests. In 1st Edition ed.; Prentice-Hall: 1968.

2. Zar, J., Biostatistical Analysis. In 2nd Edition ed.; Prentice-Hall: 1984.

3. Gartman, A.; Luther III, G. W., Oxidation of synthesized sub-micron pyrite (FeS_2) in seawater. *Geochim. Cosmochim. Acta* **2014,** *144*, 96-108.

4. Simón, M.; Martín, F.; García, I.; Bouza, P.; Dorronsoro, C.; Aguilar, J., Interaction of limestone grains and acidic solutions from the oxidation of pyrite tailings. *Environ. Pollut.* **2005,** *135*, (1), 65-72.

5. Chopard, A.; Plante, B.; Benzaazoua, M.; Bouzahzah, H.; Marion, P., Geochemical investigation of the galvanic effects during oxidation of pyrite and base-metals sulfides. *Chemosphere* **2017,** *166*, 281-291.

6. Nesbitt, H. W.; Muir, I. J., Oxidation states and speciation of secondary products on pyrite and arsenopyrite reacted with mine waste waters and air. *Mineral. Petrol.* **1998,** *62*, (1-2), 123-144.

7. Pérez-López, R.; Cama, J.; Nieto, J. M.; Ayora, C., The iron-coating role on the oxidation kinetics of a pyritic sludge doped with fly ash. *Geochim. Cosmochim. Acta* **2007,** *71*, (8), 1921-1934.

8. Bonnissel-Gissinger, P.; Alnot, M.; Ehrhardt, J.-J.; Behra, P., Surface oxidation of pyrite as a function of pH. *Environ. Sci. Technol.* **1998,** *32*, (19), 2839-2845.

9. Hood, T. A. The kinetics of pyrite oxidation in marine systems. PhD dissertation, University of Miami, Coral Gables, Florida, 1991.

10. Kresse, G.; Joubert, D., From ultrasoft pseudopotentials to the projector augmented-wave method. *Phys. Rev. B* **1999,** *59*, (3), 1758-1775.

11. Harrington, R.; Hausner, D. B.; Xu, W.; Bhandari, N.; Michel, F. M.; Brown, G. E.; Strongin, D. R.; Parise, J. B., Neutron Pair Distribution Function Study of Two-Line Ferrihydrite. *Environ. Sci. Technol.* **2011,** *45*, (23), 9883-9890.

12. Michel, F. M.; Ehm, L.; Antao, S. M.; Lee, P. L.; Chupas, P. J.; Liu, G.; Strongin, D. R.; Schoonen, M. A. A.; Phillips, B. L.; Parise, J. B., The structure of ferrihydrite, a nanocrystalline material. *Science* **2007,** *316,* (5832), 1726-1729.

13. Cismasu, A. C.; Michel, F. M.; Stebbins, J. F.; Levard, C.; Brown Jr, G. E., Properties of impurity-bearing ferrihydrite I. Effects of Al content and precipitation rate on the structure of 2-line ferrihydrite. *Geochim. Cosmochim. Acta* **2012,** *92*, 275-291.

14. Mitsunobu, S.; Takahashi, Y.; Terada, Y.; Sakata, M., Antimony(V) incorporation into synthetic ferrihydrite, goethite, and natural iron oxyhydroxides. *Environ. Sci. Technol.* **2010,** *44*, (10), 3712-3718.

15. Manceau, A.; Schlegel, M. L.; Musso, M.; Sole, V. A.; Gauthier, C.; Petit, P. E.; Trolard, F., Crystal chemistry of trace elements in natural and synthetic goethite. *Geochim. Cosmochim. Acta* **2000,** *64*, (21), 3643-3661.

16. Liu, W.; Mei, Y.; Etschmann, B.; Brugger, J.; Pearce, M.; Ryan, C. G.; Borg, S.; Wykes, J.; Kappen, P.; Paterson, D.; Boesenberg, U.; Garrevoet, J.; Moorhead, G.; Falkenberg, G., Arsenic in hydrothermal apatite: Oxidation state, mechanism of uptake, and comparison between experiments and nature. *Geochim. Cosmochim. Acta* **2017,** *196*, 144-159.

17. Qian, G.; Schumann, R. C.; Li, J.; Short, M. D.; Fan, R.; Li, Y.; Kawashima, N.; Zhou, Y.; Smart, R. S. C.; Gerson, A. R., Strategies for Reduced Acid and Metalliferous Drainage by Pyrite Surface Passivation. *Minerals* **2017,** *7*, (3), 42.